Available online at www.sciencedirect.com
SCIENCE DIRECT
Journal of Catalysis 234 (2005) 451–462
JOURNAL OF CATALYSIS
www.elsevier.com/locate/jcat

Metal–support interactions and reactivity of Co/CeO_2 catalysts in the Fischer–Tropsch synthesis reaction

L. Spadaro [a,*], F. Arena [a,b], M.L. Granados [c], M. Ojeda [c], J.L.G. Fierro [c], F. Frusteri [a]

[a] *Istituto di Tecnologie Avanzate per l'Energia "Nicola Giordano" (CNR-ITAE), Via Salita S. Lucia sopra Contesse n.5, I-98126 S. Lucia, Messina, Italy*
[b] *Dipartimento di Chimica Industriale e Ingegneria dei Materiali, Università degli Studi di Messina, Salita Sperone 31, I-98166 S. Agata (Messina), Italy*
[c] *Instituto de Catálisis y Petroleoquímica, Camino de Valdelatas s/n, Campus de la Universidad Autónoma de Madrid, Madrid 28049, Spain*

Received 24 March 2005; revised 10 June 2005; accepted 9 July 2005

Available online 11 August 2005

Abstract

The effects of the preparation method (combustion and incipient wetness) and Co loading (1–5 wt%) on the structure, redox, and morphological properties of the Co/CeO_2 system were probed by X-ray diffraction, X-ray photoemission spectroscopy, scanning electron microscopy, CO and H_2 chemisorption and temperature-programmed desorption measurements. Synthesis route and Co-loading control the structure and morphological properties, markedly affecting the reactivity of the Co/CeO_2 system in the Fischer–Tropsch synthesis (FTS) reaction ($T_R = 250\,^{\circ}C$; $P_R = 20$ atm). Both metal–support interaction(s) and Co dispersion control the strength and relative concentration of CO and H_2 adsorption sites enabling marked differences in the specific site–time–yield of the various catalysts.
© 2005 Published by Elsevier Inc.

Keywords: Co/CeO_2 catalyst; Preparation method; Metal dispersion; Reduction pattern; Structural properties; Interfacial area; Fischer–Tropsch synthesis

1. Introduction

The pressing need to reduce the environmental impact of modern technology and lifestyles imposes the need for continuous development and upgrading of old and novel methodologies aimed at a significantly reducing pollutant emissions, mainly from mobile sources, to warrant a tolerable quality of life in large metropolitan areas. This has prompted an extraordinary research effort aimed both at improving emission control systems and synthesizing more effective and cleaner fuels from syngas that have lower CO_2, NO_x, and SO_x emission levels [1–3]. In perspective, this goal embodies a strategic advance for the petrochemical industry, because it would enable the exploitation of natural gas (NG) instead of oil as raw material for fuel production, in gas-to-liquid (GTL) technology [1–5]. Synthetic gasoline obtained by Fischer–Tropsch synthesis (FTS) is in fact of great practical interest, because the very low aromatic content, absence of sulphur, and moderate distillate fraction, characterized by a high cetane number, results in superior combustion efficiency, leading to reduced CO_2 and particulate emissions from compression-ignited engines [5].

Typically, FTS catalysts include VIII group base metals (Co, Ru, Fe), with Co-based ones ensuring a superior long-chain hydrocarbon yield and longer lifetime [6–8]. Although many petrochemical companies have already patented their own know-how, with continued diversification of outlet streams [9,10] and feed composition [5,11], further improvement in FTS catalysts can be expected, mainly in terms of "narrower" product distribution [12], resistance to deactivation by fouling, and especially enhanced mechanical strength [13–15]. Because of this, such factors as particle size and shape, metal loading and dispersion, nature of the support, and type and strength of the metal–support interaction(s) have been widely assessed [7,8,16–28]. Numerous studies have been devoted to ascertaining the influence of oxide carriers (e.g., titania, silica, alumina, and zirconia) on the activity and stability of Co catalysts [17–22], and have

* Corresponding author. Fax: +39-090-624247.
E-mail address: lorenzo.spadaro@itae.cnr.it (L. Spadaro).

0021-9517/$ – see front matter © 2005 Published by Elsevier Inc.
doi:10.1016/j.jcat.2005.07.006

determined that the "site time yield" of Co-based catalysts is not affected by either the degree of dispersion or the support identity [17,27,28].

The effects of ceria, as either a promoter or a support, seem rather controversial, because both solid-state interactions and enhanced reactivity toward the gas phase [23,25] affect the redox and electronic properties of the active phase, shaping a singular adsorption behavior reflected in unusual catalytic features of active phases [24,25]. In particular, an enhanced reducibility and surface affinity of ceria for both H_2 and CO molecules [23,25] might well contribute to shaping the reactivity of the Co/CeO_2 system in FTS [25]. Then, controlling the "intimacy" of contact between support and active phase, the synthesis route could exert a basic influence on the physicochemical properties and reactivity of the final catalyst [26].

Consequently, this paper is aimed at assessing structural, redox, and catalytic properties of differently loaded (1–5 wt%) Co/CeO_2 systems obtained by the conventional incipient wetness technique and the combustion method, reported by Bera et al. [29,30]. A systematic evaluation of the activity pattern of the various systems in the FTS in the light of the relative adsorption properties provides some structure–activity relationships highlighting the fundamental effects of metal–support interactions and dispersion on the reactivity of the Co/CeO_2 system.

2. Experimental

2.1. Materials

Differently loaded (1–5 wt%) ceria-supported Co catalysts were synthesized by either incipient wetness (*-iw*) or combustion routes (*-cb*) [29,30]. Incipient wetness catalysts were prepared by the stepwise addition of a $Co(NO_3)_2{\cdot}6H_2O$ (Aldrich; >98%) aqueous solution to a powder CeO_2 sample obtained by the combustion method.

Combustion catalysts were obtained by placing in a ceramic dish an aqueous solution of $(NH_4)_2Ce(NO_3)_6{\cdot}9H_2O$ (Aldrich; 99.9%), $Co(NO_3)_2{\cdot}6H_2O$ and oxaldihydrazide (Aldrich; >98% reagent) as fuel. The dish was then introduced into a muffle furnace preheated to 420 °C. After boiling, the solution ignited, producing a "cold flame" that yielded a spongelike solid [29,30]. At the end of the combustion process, the temperature was kept constant for 1 h at 420 °C and then decreased to room temperature during 24 h.

To assess the effect of the reducing agent (fuel) on the structure of combustion catalysts, a 4% Co/CeO_2 sample [4(Urea)-*cb*] was synthesised using urea instead of oxaldihydrazide. The samples studied are listed in Table 1.

Table 1
List of the studied catalysts

Code	Preparation method	Co (wt%)	SA_{BET} ($m^2\,g^{-1}$)
1(ODH)-*cb*	Combustion (ODH)	0.92	3.5
2(ODH)-*cb*	Combustion (ODH)	1.96	1.8
4(ODH)-*cb*	Combustion (ODH)	3.96	0.9
5(ODH)-*cb*	Combustion (ODH)	5.13	1.0
4(Urea)-*cb*	Combustion (Urea)	4.28	30.0
4-*iw*	Incipient wetness	4.47	13.0

2.2. Methods

X-ray photoemission spectroscopy (XPS) analysis of catalysts was performed in high-resolution mode using a Physical Electronics GMBH PHI 5800-01 spectrometer equipped with an X-ray Al monochromated anode source (Al-K_α radiation), at a beam power of 350 W, and a hemispherical electron analyzer of 150 mm. The samples were analyzed in ESCA multiplex mode, in the regions 770–810 eV (Co $2p_3$), 280–300 eV (C 1*s*), 525–540 eV (O 1*s*), and 870–935 eV (Ce 3*d*), using a pass energy of 46.95 eV for elemental analysis and 11.75 eV for determination of the oxidation number. The binding energy (BE) was calibrated taking the C 1*s* photoelectron peak (284.8 eV) of "adventitious" carbon as a reference. Before measurements, powdered samples were kept in the preparation chamber for 24 h at 6.0×10^{-8} Torr and then introduced into the ultra-high-vacuum (10^{-9} Torr) analysis chamber. XPS data were processed by the PHI MULTIPAK 6.1 software and the PHI Handbook of XPS [31].

X-ray diffraction (XRD) analysis of powdered catalyst samples was done using a Philips X-Pert diffractometer operating with Ni β-filtered Cu-K_α radiation at 40 kV and 30 mA. Continuous scans were collected with scan rates of $0.5°\,min^{-1}$ and $0.05°\,min^{-1}$ in the 2θ ranges 5°–100° and 35°–45° and 60°–70°, respectively. The particle size of ceria and cobalt oxide was determined by Scherrer's equation, assuming a Gaussian shape of the peaks.

Scanning electron microscopy (SEM) analyses were carried out with a Jeol 5600 LV microscope, operating with an accelerating voltage of 20 kV. SEM micrographs were taken after coating by gold sputtering.

Temperature-programmed reduction (TPR) in the range 0–1000 °C was performed in a flow apparatus operating in both pulse and continuous modes using a linear quartz microreactor (i.d., 4 mm; length, 200 mm) fed with a 5.0% H_2/Ar mixture flowing at 30 STP $cm^3\,min^{-1}$ and with a heating rate of $20\,°C\,min^{-1}$. The sample weight was set to keep the Co load constant (2.0–2.5 mg), avoiding mass and heat-transfer limitations. Hydrogen consumption was monitored by a thermoconductivity detector (TCD) connected to a PC for data storage and processing. The TCD response was quantitatively calibrated by monitoring the reduction of known amounts of CuO. Under such condition, TPR was reliable and accurate in terms of both peak position (±5 °C) and hydrogen consumption (±5%).

Modeling of TPR spectra was performed through deconvolution analysis of experimental profiles by a linear combi-

nation of Gaussian components, using the PeakFit version 4 software package (Jandel Scientific) [32].

CO uptake measurements were performed in a pulse mode using He as carrier gas (30 STP $cm^3\,min^{-1}$) as described previously [33]. Before measurement, catalyst samples were reduced under a 10% H_2/N_2 flow (100 $cm^3\,min^{-1}$) for 1 h at 400 °C and then flushed at the same temperature (20 min) in the He carrier flow. After cooling to room temperature, CO pulses (0.5 μmol) were injected onto the sample until saturation was reached. Metal dispersion was calculated assuming a CO:Co chemisorption stoichiometry equal to 1, whereas a surface density of 14.6 Co atoms nm^{-2} was assumed for metal surface area (MSA) evaluation [34]. The θ parameter, calculated as the normalized ratio of MSA divided by the difference between total and MSA (e.g., $MSA/(SA_{BET} - MSA)$), is taken as a measure of the interfacial Co–CeO_2 area.

CO-TPD measurements on the saturated samples were carried out in a temperature range of 20–300 °C using He as carrier gas flowing at 30 $cm^3\,min^{-1}$ and a heating rate of 20 °C min^{-1}.

H_2 temperature-programmed desorption (H_2-TPD) was performed after an in situ activation treatment of the catalysts under a 10% H_2/N_2 flow (100 $cm^3\,min^{-1}$) for 1 h at 400 °C, with further saturation under flowing hydrogen at room temperature for 10 min and then at −80 °C for 5 min. H_2-TPD measurements were made in a temperature range of −80–800 °C, using Ar as carrier gas (30 $cm^3\,min^{-1}$) with a heating rate of 20 °C min^{-1}. The calibration of the peak area was done by pulse injection of known volumes of hydrogen into the carrier gas [33].

Catalyst testing in the FTS reaction was performed at 250 °C and a total pressure of 20 atm, using a "down flow" fixed-bed SS reactor (i.d., 6 mm; length, 200 mm) containing 0.5 g of catalyst diluted with 1.5 g of CSi and fed with a $H_2/CO/N_2 = 64:32:4$ reaction mixture at the rate of 50 STP $cm^3\,min^{-1}$ (GHSV, 6000 $cm^3\,g^{-1}\,h^{-1}$). Catalyst samples were reduced in situ at 400 °C for 1 h under a 10% H_2/N_2 flow (100 STP $cm^3\,min^{-1}$), then cooled in flowing H_2/N_2 at 250 °C. The reaction temperature was monitored by a thermocouple inserted into the catalyst bed. Reagents and products were analyzed using an HP 5890 gas chromatograph equipped with SPB-5 and a Carboplot-Q columns, connected to thermal conductivity and flame ionization detectors for detecting permanent gases, hydrocarbons, and oxygenates.

3. Results

3.1. Structural properties

Combustion catalysts ((ODH)-*cb*) obtained using oxaldihydrazide as fuel are characterized by quite low surface area values (Table 1), decreasing with the Co loading from 4 to 1 $m^2\,g_{cat}^{-1}$. The 4-*iw* sample features a comparatively larger surface area (13 $m^2\,g^{-1}$), whereas using urea instead of oxaldihydrazide in the combustion synthesis route [4(Urea)-*cb*] produces the largest SA_{BET} (30 $m^2\,g^{-1}$), higher by more than one order of magnitude than that of the 4(ODH)-*cb* sample (1 $m^2\,g_{cat}^{-1}$).

Some peculiar differences in the XRD patterns of the "highly loaded" Co/CeO_2 systems (Fig. 1) further account for the specificity of the preparation method on the catalyst structure. Both the 4(ODH)-*cb* and 4-*iw* samples present very sharp diffraction lines in the 2θ range 20°–100°, typical of the cerianite with a fluorite-like structure [35], along

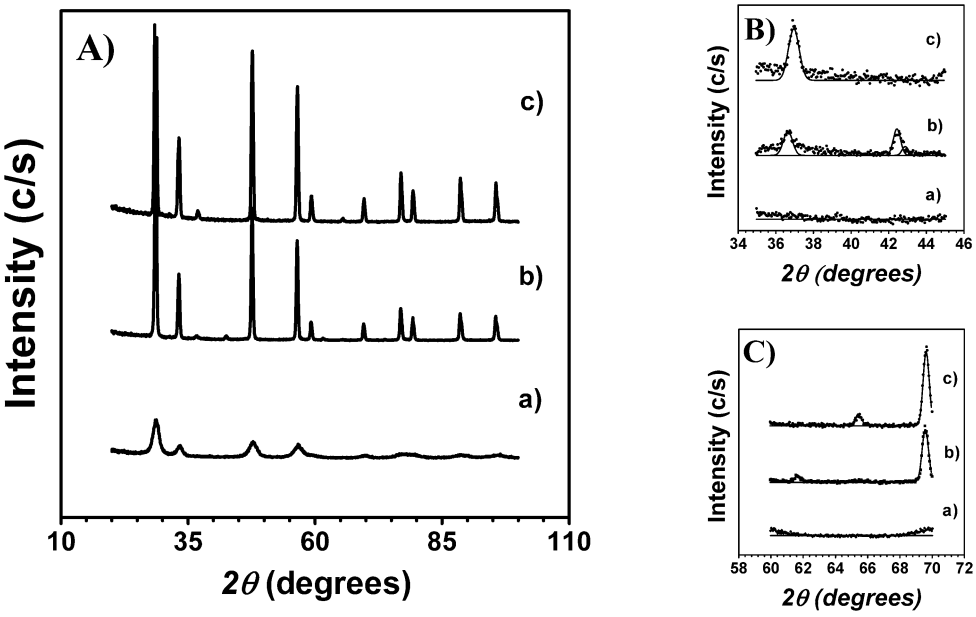

Fig. 1. X-ray diffraction patterns of the catalysts 4(Urea)-*cb* (a), 4(ODH)-*cb* (b) and 4-*iw* (c) in different 2θ ranges: 20°–100° (A), 35°–45° (B) and 60°–70° (C), respectively.

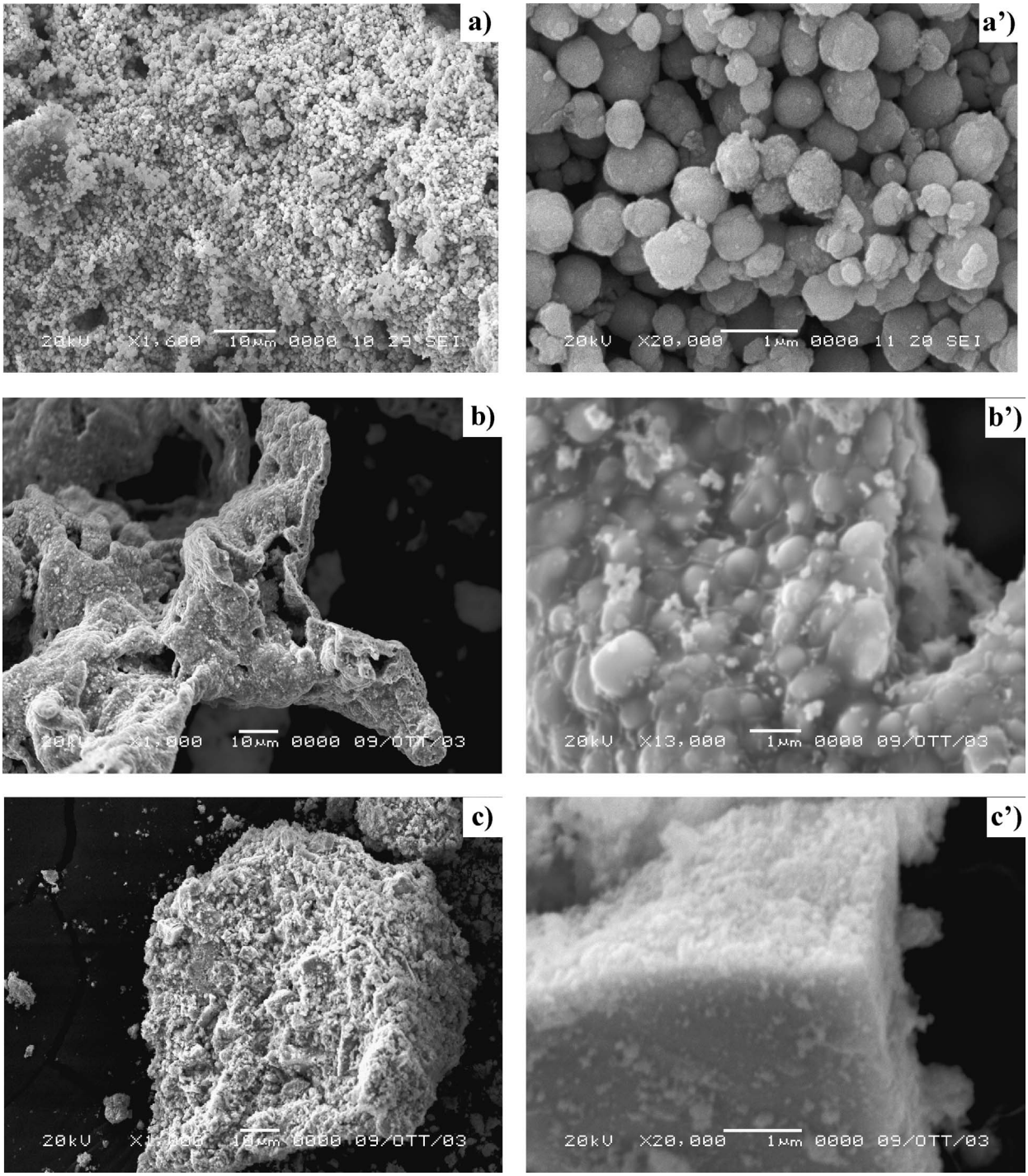

Fig. 2. SEM pictures of samples 4(Urea)-*cb* (a, a′), 4(ODH)-*cb* (b, b′) and 4-*iw* (c, c′), at different magnifications.

quite less intense reflexes in the 2θ range 35°–45° and 60°–70°(Figs. 1B and 1C), attributable to the monoclinic CoO [4(ODH)-*cb*] and cubic Co_3O_4 (4-*iw*) phases [36,37], respectively. In contrast, the XRD pattern of the 4(Urea)-*cb* sample outlines only the diffraction lines of the ceria carrier, although it is much "broader" and less intense than for previous samples. This different peak shape signals a noticeable decrease in ceria particle size from an average value of around 300 to 60 Å (plane ⟨111⟩ at 2θ equal to 28.55), whereas the Co precursor is likely present in an amorphous state and/or with a relatively high dispersion on the ceria carrier.

SEM images displayed in Fig. 2 indicate that the catalyst morphology is also closely related to the preparation method. The 4-*iw* catalyst features a quite "smooth" particle shape (Fig. 2c), although at higher magnification, the crystalline structure of the support is rather evident (Fig. 2c′). At lower magnification (Fig. 2b), the 4(ODH)-*cb* sample looks

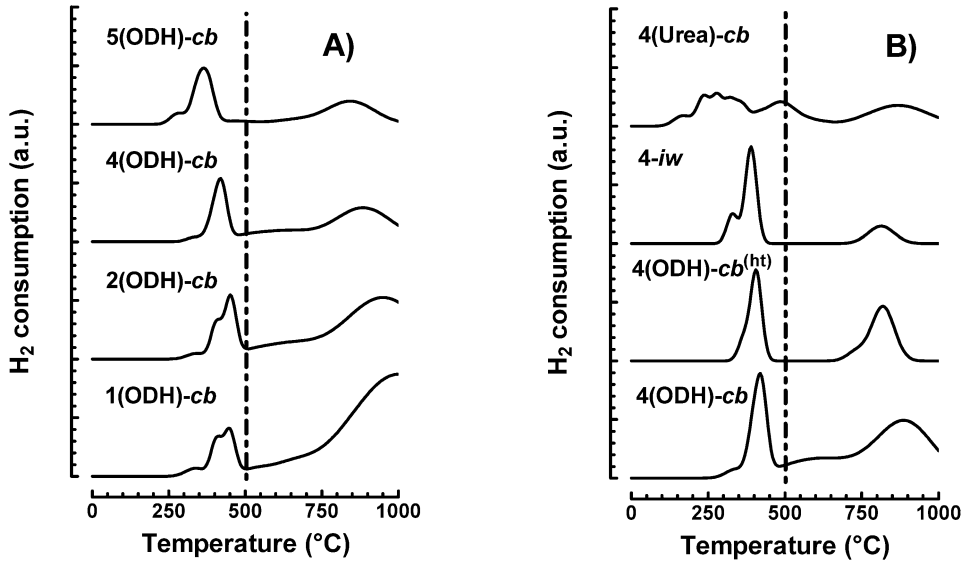

Fig. 3. TPR profiles of the catalysts. Effects of the cobalt loading (A) and preparation method (B).

Table 2
TPR data of the catalysts[a]

Sample	$T_{0,red}$ (°C)	Low temperature range (LT)			H_2/Co	High temperature range (HT)		H_2/Ce
		T_{M_1} (°C)	T_{M_2} (°C)	T_{M_3} (°C)		T_{M_4} (°C)	T_{M_5} (°C)	
1(ODH)-*cb*	275	328	408	446	1.02	640	980	0.26
2(ODH)-*cb*	269	327	405	450	1.14	636	934	0.34
4(ODH)-*cb*	260	323	408	–	1.09	640	885	0.38
4(ODH)-*cb*$^{(ht)}$	320	–	407	–	1.29	–	814	0.21
5(ODH)-*cb*	210	280	361	–	1.12	655	846	0.23
4(Urea)-*cb*	100	161	234	323	1.11	532	869	0.22
4-*iw*	280	329	387	–	1.26	–	810	0.06

[a] $T_{0,red}$ and T_{M_i} refer to the onset temperature of reduction and temperature of peak maximum. Sample 4(ODH)-*cb*$^{(ht)}$ has been subjected to a calcination treatment at 900 °C for 3 h.

very "rough" and irregular, being the result of extensive "sticking" of small grains into large agglomerates (Fig. 2b′). The structure of the 4(Urea)-*cb* catalyst looks similar to that of the 4-*iw* sample (Fig. 2a), although a more detailed observation (Fig. 2a′) reveals that it consists of an array of small spherical particles forming an intricate network of different-sized (0.1–1 μm) macropores.

3.2. Reduction pattern

The TPR profiles of Co/CeO_2 catalysts, with reference to the Co loading and preparation method, are shown in Fig. 3. The related onset temperature of reduction ($T_{0,red}$), the temperature of peak maximum (T_{M_i}), and the extent of H_2 consumption, expressed as the ratio of H_2 molecules consumed per Co (low-temperature [LT] range) or Ce (high-temperature [HT] range) atom, are summarized in Table 2.

As a rule, all of the TPR profiles (Fig. 3) consist of two regions of H_2 consumption, spanning the ranges 250–500 °C (LT) and 500–1000 °C (HT), associated with a reduction in the Co precursor(s) and ceria carrier, respectively [25,38–45]. Regardless of the loading, the TPR profiles of the combustion catalysts (Fig. 3A) display a main reduction peak centered at 420–450 °C (LT) convoluted with other poorly resolved components on the LT side with maxima at around 400 and 335 °C, respectively. The relative peaks area accounts for an H_2 consumption corresponding to an H_2/Co value ranging from 1.02 [1(ODH)-*cb*] to 1.12 [5(ODH)-*cb*]. An incipient H_2 consumption in the range 500–750 °C gives rise to a broad (unless symmetric) peak with a maximum centered between 900 °C [4(ODH)-*cb*] and 1000 °C [1(ODH)-*cb*], whose intensity (HT) corresponds to a H_2/Ce ratio between 0.23 and 0.38 (Table 2).

A comparison of the TPR spectra of similarly loaded (4 wt%) Co/CeO_2 systems obtained by different routes and/or subjected to an additional calcination treatment at 900 °C for 3 h [4(ODH)-*cb*$^{(ht)}$], is outlined in Fig. 3B. The HT calcination treatment at 900 °C affects the TPR pattern of the 4(ODH)-*cb* system, mainly causing a sharpening of both LT and HT reduction peaks, the maximum of which also shifts slightly to lower temperature. In addition, the low hydrogen consumption in the range 500–750 °C present in the spectra of the untreated systems is no longer observable. From a quantitative standpoint, the H_2/Co ratio stays almost

Table 3
H_2, CO chemisorption and XPS analysis of the catalysts

Sample	H_2 chemisorption ($\mu mol\ g_{cat}^{-1}$)	CO chemisorption			XPS[a]
		$\mu mol\ g_{cat}^{-1}$	D_{Co}[b] (%)	θ[c]	Co_{at}/Ce_{at}
1(ODH)-*cb*	3.0	1.7	1.2	0.023	0.09
2(ODH)-*cb*	13.4	2.7	0.8	0.064	0.24
4(ODH)-*cb*	18.0	1.9	0.3	0.090	0.36
5(ODH)-*cb*	14.0	1.8	0.2	0.076	0.29
4(Urea)-*cb*	352.2	97.0	13.4	0.155	0.56
4-*iw*	69.0	16.0	2.1	0.054	0.21

[a] Estimated on Co 2*p* and Ce 3*d* core level contribution, respectively.
[b] The cobalt dispersion (D_{Co}) was calculated as $[(mol_{CO_{adsorbed}}/mol_{Co})\times 100]$.
[c] The index of the cobalt–CeO_x interfacial area (θ), was calculated as $[MSA/(SA_{BET} - MSA)]$.

unchanged (1.14–1.29), whereas the H_2/Ce ratio decreases from 0.38 to 0.21 (Table 2). The TPR profile of 4-*iw* features a LT reduction pattern similar to that of the 4(ODH)-*cb* system, whereas a much lower rate of H_2 consumption (0.06) is recorded in the HT region (H_2/Ce). According to XRD data indicating the absence of a crystalline CoO_x phase (Fig. 1), the 4(Urea)-*cb* sample displays a peculiar reduction profile in the LT region, where a very broad band of H_2 consumption with several poorly resolved maxima signals a H_2/Co ratio comparable with that of the previous systems (Table 2). The H_2/Ce value is yet intermediate between those of the 4(ODH)-*cb* and 4-*iw* samples (Table 2).

3.3. Surface properties

The surface properties of the catalysts were investigated by XPS, H_2 and CO uptake measurements; the results are summarized in Table 3. All of the catalysts are characterized by larger XPS Co/Ce atomic ratio values than were expected from the bulk composition (Table 1), with the index of generalized surface Co enrichment rising with loading and the highest on the 4(Urea)-*cb* sample.

However, the very low CO uptake (1.7–2.7 $\mu mol\ g_{cat}^{-1}$) of the (ODH)-*cb* catalysts accounts for metal dispersion values between 0.2 and 1.2%. Mirroring a greater development of total surface area (Table 1), the 4-*iw* system features a considerably greater CO uptake (16 $\mu mol\ g_{cat}^{-1}$), corresponding to only a slight increase in metal dispersion (2%). At least, the catalyst 4(Urea)-*cb*, characterized by the largest SA_{BET}, features the maximum CO uptake (97 $\mu mol\ g_{cat}^{-1}$), which accounts for the highest metal dispersion value (13.4%) in the series. Because of the variable MSA and SA_{BET}, the θ parameter ranges between a minimum of about 0.02 and a maximum of 0.16 (Table 3).

The CO-TPD spectra of the 4(ODH)-*cb* and 4(Urea)-*cb* catalysts, shown in Fig. 4A, besides accounting for the latter catalyst's much greater chemisorption capacity, also indicates marked differences in the desorption pattern attributable to different populations of active sites. In particular, the TPD spectrum of the 4(Urea)-*cb* sample displays two convoluted desorption peaks, centered at around 110 and 165 °C, with an overwhelming intensity of the latter. In contrast, the

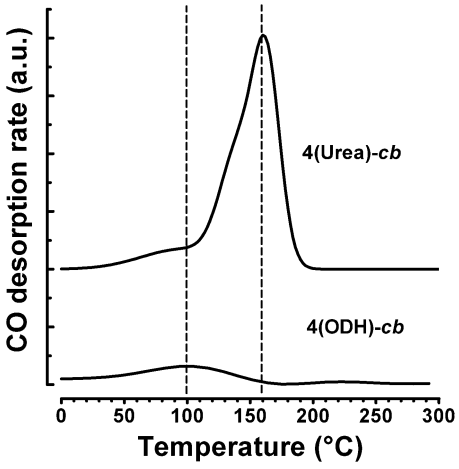

(A)

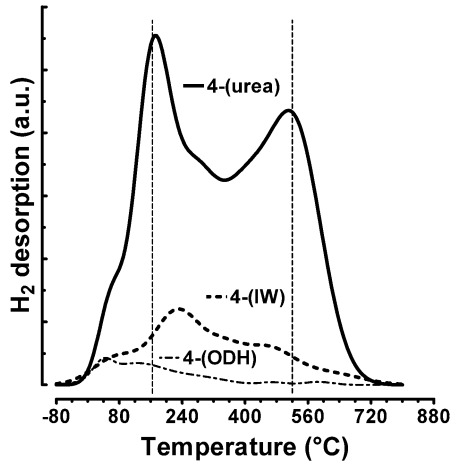

(B)

Fig. 4. CO-TPD (A) and H_2-TPD (B) spectra of various catalysts.

occurrence of only one desorption peak at lower temperature, with an intensity and position matching the LT peak of the previous sample, points to the presence of only weak adsorption sites on the poorly dispersed 4(ODH)-*cb* system.

Different surface properties of the various catalysts were also probed by the TPD profiles of preadsorbed hydrogen, shown in Fig. 4B. In a qualitative agreement with the dispersion scale derived from CO uptake measurements, the most widely dispersed catalysts [i.e., 4(Urea)-cb and 4-iw] display

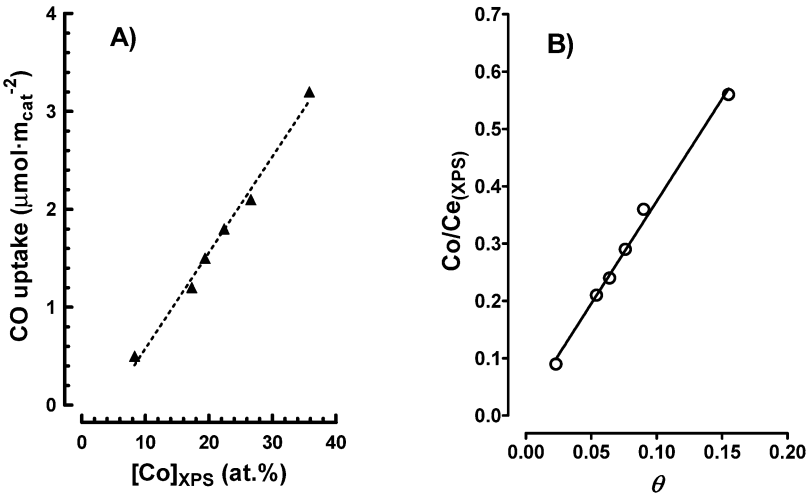

Fig. 5. Relationship between CO uptake and XPS data. CO uptake vs $[Co]_{XPS}$ atomic ratio (A) and $Co/Ce_{(XPS)}$ atomic signal intensity vs θ parameter (B).

Table 4
FTS catalytic activity data at 250 °C (P_R: 20 bar, GHSV: 6000 $cm^3\ g_{cat}^{-1}\ h^{-1}$)

Sample	Activity			Selectivity (% carbon basis)			
	O/Co[a]	X_{CO} (%)	α[b]	C_1	C_2–C_4	C_{5+}	Oxygenates
1(ODH)-*cb*	0.9	1.90	0.67	8.7	45.1	39.1	7.1
2(ODH)-*cb*	0.9	8.20	0.69	7.9	42.8	43.4	5.9
4(ODH)-*cb*	1.0	16.40	0.72	9.0	42.1	44.2	4.7
5(ODH)-*cb*	1.1	9.80	0.62	11.4	37.0	46.5	5.3
4(Urea)-*cb*	1.5	1.60	0.43	23.7	35.1	16.7	24.5
4-*iw*	1.4	5.50	0.66	11.8	37.6	43.5	7.1

[a] Calculated by pulse titration measurements at 400 °C on fresh samples after the standard reduction procedure.
[b] Calculated on the basis of Schulz–Flory equation.

an overwhelming intensity of the peak areas in comparison to the 2(ODH)-*cb* and 4(ODH)-*cb* samples, corresponding to H_2 uptake values between 1 and 352 μmol g_{cat}^{-1} (Table 3), with marked differences in terms of position and relative intensity of the desorption peaks also evident. The most widely dispersed systems present a similar desorption pattern in the range 0–720 °C, with an almost balanced contribution of the peak areas below and above 300 °C. In contrast, both the 4-(ODH) and 2-(ODH) catalysts feature a prevailing desorption at low temperature with a very low amount (if any) of hydrogen released at >300 °C (Fig. 5).

3.4. Catalytic activity

Steady-state activity data (e.g., after 50 h) of the various catalysts in the FTS reaction at 250 °C are summarized in Table 4 in terms of CO conversion (X_{CO}), product selectivity, and chain-growth probability (α). The data of O_2 titration measurements at 400 °C of the catalysts reduced according to standard procedure and given in Table 4 in terms of O/Co ratio signal that the degree of reduction in the active phase is always close to the stoichiometric value (0.9–1.1) for the (ODH)-*cb* systems, whereas some contribution of the reduced ceria matrix likely leads to supra-stoichiometric O/Co values (1.4–1.5) on the 4-*iw* and 4(Urea)-*cb* samples [25].

The (ODH)-*cb* catalysts feature an increasing activity with the Co loading until a maximum of 4 wt%, thereafter (5(ODH)-*cb*) lowering to a level similar to that of the 2(ODH)-*cb* system in concomitance with a decrease of α to its lowest value (Table 4). The selectivity is almost independent of the loading (and conversion), with an overall hydrocarbon yield >90% (Table 4). In particular, the 1(ODH)-*cb* sample has the poorest performance, with a X_{CO} value of only around 2%, whereas the 4(ODH)-*cb* sample has the highest X_{CO} (16.4%) along with the best chain growth probability (0.72).

Comparing the activity–selectivity pattern of similar loaded catalysts prepared by different routes indicates that the 4(Urea)-*cb* catalyst exhibits the worst catalytic performance, as evidenced by a strong decrease in both activity (X_{CO}, 1.6%) and long-chain hydrocarbon selectivity (around 50% to C_{2+}), with the latter mirroring a α value of only 0.42 (Table 4). The catalyst prepared by incipient wetness (4-*iw*) exhibits performance between that of the foregoing two systems in terms of activity (X_{CO}, 5.5%) and hydrocarbon selectivity (around 93%), with a value of α similar (0.66) to those of the (ODH)-*cb* systems (Table 4).

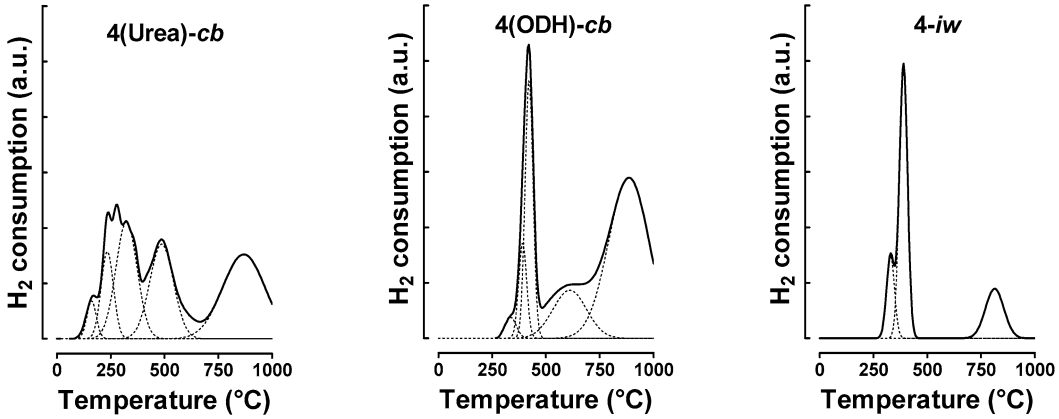

Fig. 6. Deconvolution analysis of TPR spectra of the catalysts 4(Urea)-*cb*, 4(ODH)-*cb* and 4-*iw*.

4. Discussion

4.1. Physicochemical properties

Although Bera et al. emphasised the valuable effects of the combustion route on enhancing the dispersion of active phases on various oxide carriers [29,30,46], different structural features indicate a critical influence of the fuel on the efficiency of the synthesis route. In particular, the low surface area value of the (ODH)-*cb* series can be tentatively explained by the lower solubility of the oxaldihydrazide into the precursor solution. SEM analysis in fact reveals that the large surface area of the 4(Urea)-*cb* system arises from an interparticle porosity, which is absent in the 4(ODH)-*cb* sample. Then a homogeneous solution of oxide precursors and urea, leading to the development of huge amounts of gaseous products (e.g., N_2, CO_2, H_2O, NO_x) during combustion, would prevent the coalescence of nascent oxide particles in the 4(Urea)-*cb* sample. In contrast, effective separation of the catalyst particles would be hindered during the combustion of the oxaldihydrazide as a poorly homogeneous mixing into the oxide precursors solution (Fig. 2). Such marked differences in total surface area evidently imply quite different properties of the active phase of the (ODH)-*cb* and 4(Urea)-*cb* systems (Table 3). Considering the main structural features of the preshaped support, the incipient wetness route ensures SA_{BET} and metal dispersion values between those of the (ODH)-*cb* and (Urea)-*cb* samples. In any case, a general relationship between the surface CO uptake ($\mu mol\, m_{cat}^{-2}$) and the XPS Co atomic concentration ($[Co]_{XPS}$) of all of the studied catalysts (Fig. 5A) leads us to exclude relevant SMSI-type effects induced by the reduction treatment. In addition, comparing the Co/Ce_{XPS} atomic ratio with the θ parameter (Fig. 5B), evaluated from CO chemisorption (Table 3), the excellent straight-line relationship confirms the reliability of the latter in providing a measure of the Co–CeO_2 interfacial area. Such data prove that the reduction treatment does not modify the dispersion of the Co precursor over the ceria carrier to any significant extent [25].

Other structural features denote the peculiarity of the combustion route. In particular, because CoO is not stable at a temperature $>300\,^{\circ}C$ in the presence of oxygen [40], its formation (instead of the more stable Co_3O_4 cubic phases) on the 4(ODH)-*cb* catalysts would be a consequence of unsteady-state conditions during synthesis. However, transformation of the monoclinic CoO particles into Co_3O_4 crystallites with a cubic structure is enabled by calcination at $900\,^{\circ}C$.

All of the aforementioned structural differences evidently imply different reduction patterns. Nevertheless, according to Arnoldy and Moulijin [40], the details of the Co–CeO_2 interaction are not straightforward from "rough" TPR profiles (Fig. 3), because several factors can simultaneously affect the reduction of Co-based catalysts. In an attempt to overcome such drawbacks, the TPR spectra were analyzed by a mathematical fitting program and deconvoluted into Gaussian components, each of which could be related to the reduction of a definite Co^{n+} species based on the assumption of a normal distribution of activation energy for reduction [32]. A preliminary iterative procedure determined that all of the spectra result from the linear combination of five Gaussian components characterized by the same center position (M, °C) and full width at half-maximum (fwhm, °C). Representative results of the deconvolution analysis of TPR spectra of the 4(Urea)-*cb*, 4(ODH)-*cb*, and 4-*iw* systems are shown in Fig. 6, and the Gaussian parameters of all spectra are summarized in Table 5. The fact that all of the components remain almost unchanged in terms of position and fwhm can be taken as a reasonable proof of the similar nature and reactivity of Co species in the various samples [32]. In particular, on the basis of literature findings [25,39–45] and taking into account the XRD data and the effects of the calcination treatment, Co loading, and preparation method on the intensity of the various components (Table 5), the following assignment is tentatively made:

Peak 1 Reduction of the Co_3O_4 phase (amorphous or crystalline) to CoO.

Table 5
Fitting parameter of TPR spectra

Sample	Low temperature range (LT)						High temperature range (HT)			
	M_1/fwhm$_1$ (°C/°C)	A_1 (H_2/Co)	M_2/fwhm$_2$ (°C/°C)	A_2 (H_2/Co)	M_3/fwhm$_3$ (°C/°C)	A_3 (H_2/Co)	M_4/fwhm$_4$ (°C/°C)	A_4 (H_2/Ce)	M_5/fwhm$_5$ (°C/°C)	A_5 (H_2/Ce)
1(ODH)-*cb*	337/65	0.15	406/45	0.38	449/45	0.49	644/170	0.01	1000/200	0.25
2(ODH)-*cb*	339/65	0.13	406/45	0.36	452/45	0.65	646/170	0.06	950/200	0.26
4(ODH)-*cb*	336/65	0.08	392/45	0.27	422/45	0.74	641/170	0.10	885/200	0.28
5(ODH)-*cb*	280/65	0.13	347/45	0.42	380/45	0.57	659/170	0.05	844/200	0.18
4-*iw*	329/65	0.29	389/45	0.97	–	–	–	–	813/200	0.06
4(ODH)-*cb*$^{(ht)}$[a]	367/65	0.26	407/45	1.03	–	–	–	–	819/200	0.21
4(Urea)-*cb*	161/50	0.19	234/70	0.32	323/110	0.59	532/180	0.09	869/210	0.13

[a] Sample 4(ODH)-*cb*$^{(ht)}$ has been subjected to a calcination treatment at 900 °C for 3 h.

Peak 2 Reduction of CoO particles (coming from Co_3O_4 reduction and/or present in an amorphous/crystalline phase) to Co^0.
Peak 3 Reduction of small CoO clusters and/or Co^{II} ions interacting with CeO_2.
Peak 4 Reduction of surface CUS Ce^{IV} ions.
Peak 5 Reduction of bulk Ce^{IV} ions.

Literature data on the reduction of Co_3O_4 are rather controversial, because the appearance of the $Co_3O_4 \rightarrow CoO \rightarrow Co^0$ reduction steps in TPR measurements depends strongly on the experimental conditions, catalyst composition, and perhaps dispersion of the active phase [25,39–45]. For instance, stepwise reduction was not evident for Al_2O_3-supported Co [40,41] and Co–CeO_2/SiO_2 [45] catalysts, whereas Bruce et al. [45] reported that the reduction of the Co_3O_4 spinel to Co^0 in Co/CeO_2 catalysts proceeds in two steps, the maxima of which occur at around 300 and 400 °C, respectively. The third component stems from the reduction of Co^{2+} ions in a strong interaction with the ceria matrix [45], whereas the fourth component, present only in the spectra of combustion catalysts (Fig. 6), monitors the reduction of (surface) Ce^{IV} ions interacting with Co^{2+} ions [23,25,38]. The concentrations of these latter two species are in fact directly related, as indicated by the linear relationship between the intensity of the third and fourth components of combustion catalysts, shown in Fig. 7. As the inadequacy of the incipient wetness route in ensuring an effective dispersion of the Co precursor through the carrier, preventing the stabilization of these species on the 4-*iw* system (Fig. 7), this relationship indicates the reduction of about six surface Ce^{IV} ions for each Co^{2+} ion. Finally, the intensity of the fifth component is associated with the reduction of Ce^{IV} ions in the bulk of ceria particles and is virtually unaffected by the presence of the active phase [23,25,38]. Some slight shift in the relative maximum position (Table 5) mirrors only the different amounts of catalyst used in TPR measurements (see Section 2). Low (if any) surface reducibility of ceria, as evidenced by complete disappearance of the fourth and third peaks (Fig. 3B), thus accounts for the catalyst reconstructuring induced by the calcination treatment at 900 °C [4(ODH)-*cb*$^{(ht)}$]. In addition, the greater intensity of the first

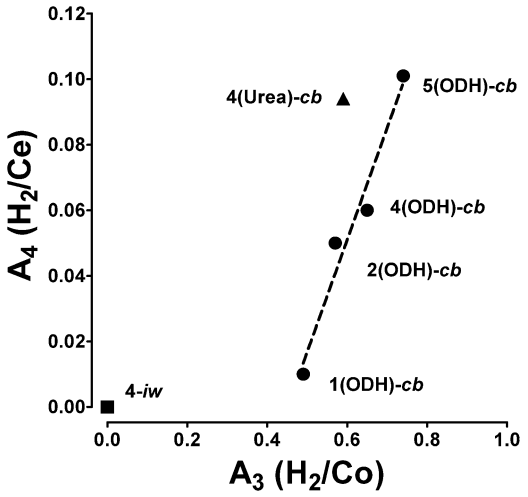

Fig. 7. Relationship between the intensity of 3rd and 4th Gaussian components from modelling of TPR spectra.

two components in the LT (Table 5) matches with the transformation of CoO/Co^{2+} species into the more stable Co_3O_4 phase [47].

The peculiar TPR pattern of the 4(Urea)-*cb* sample deserves consideration, being the consequence of a much wider dispersion of the active phase (Table 3). In this case, the typical components of crystalline Co oxide(s) are hardly (if at all) visible, because the overwhelming contribution of components arising from the reduction of well-dispersed Co^{n+} ions. Deconvolution analysis of this system indicates a marked shift to lower temperature of the components relative to the reduction of the supported phase, evidently prompted by enhanced reactivity with respect to bulk oxide particles (Table 5).

The large dispersion range spanned by the various catalysts also evidently implies a different structure of the surface metal sites, as evidenced by the marked changes in both CO (Fig. 4A) and hydrogen (Fig. 4B) desorption patterns. Indeed, in concordance with very low metal dispersion, the TPD patterns of the 4(ODH)-*cb* catalyst indicate only weak chemisorption sites, likely located on high-index planes of large Co particles, whereas the TPD patterns of the 4(Urea)-*cb* sample feature a prevailing concentration of

strong chemisorption sites linked to a greater degree of coordinative unsaturation in small metal crystallites. Therefore, rather different surface and structural properties account for the catalytic behavior of the various systems in the FTS reaction.

4.2. Structure–activity relationships

Since the discovery of the FTS on cobalt catalysts at the start of the twentieth century, much research has focused on improving process targets, particularly in concordance with a growing interest in GTL technology over the last two decades [3,17,27,28]. Although the superior performance of Co catalysts is generally recognized [6], several aspects of reaction mechanism and catalyst requirements remain matters of debate [27,28,48]. In particular, given the structure-insensitive character of the FTS on Co-based catalysts [17,27,28], most attempts to improve process performance were pursued through the optimization of catalyst structure and composition, reducibility of the active phase [49], and reactor design [17,27,28,50]. However, studying the influence of dispersion on the activity–selectivity pattern of differently loaded (3–10 wt%) Co/Al_2O_3, Co/SiO_2, and Co/TiO_2 catalysts, Reuel and Bartholomew found that turnover frequency (TOF) depends on the support, dispersion, metal loading, and preparation method [51,52]. TOF values between 2.2 and 38 $\times$ 10^{-3} s^{-1} were reported for 10 wt% Co/Al_2O_3, Co/C, Co/MgO, and Co/TiO_2 systems, although the same authors concluded that SMSI interference could have led to unreliable estimates of the number of Co surface sites [52].

Consequently, given the numerous factors shaping the catalytic pattern of Co systems, it is difficult to determine general rules that fully account for the various effects documented throughout the vast literature [17–22,39–45,48–54]. Moreover, some peculiar aspects of the reactivity can be related to the simultaneous occurrence of several ongoing modifications induced by the reaction system on the structural properties of the catalyst. For instance, superior performance of the Co catalyst has often been found for a high degree of catalyst reduction attained in "diluted" systems at much higher temperatures than for highly loaded ones [49]. Complete reduction implies relatively poor dispersion of the active phase due to high-temperature reduction treatment or metal loading [49]. Moreover, relatively inert oxide materials used as carriers for catalyst preparation do not display significant reactivity toward reagent molecules at typical FTS conditions, whereas cerium oxide(s) exhibits enhanced reactivity toward both H_2 and CO [23,25,38,53]. Indeed, Shi et al. [55] recently showed that the addition of CeO_2 enhances cobalt dispersion as well as the activity and selectivity of Co/SiO_2 catalysts. Although these authors did not report any quantitative estimate of the cobalt dispersion, they concluded that the best activity–selectivity pattern is linked to an optimum Co/Ce atomic ratio [55].

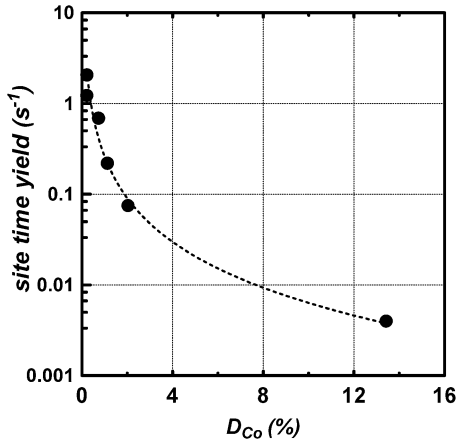

Fig. 8. Site–time–yield vs Co dispersion (D_{Co}).

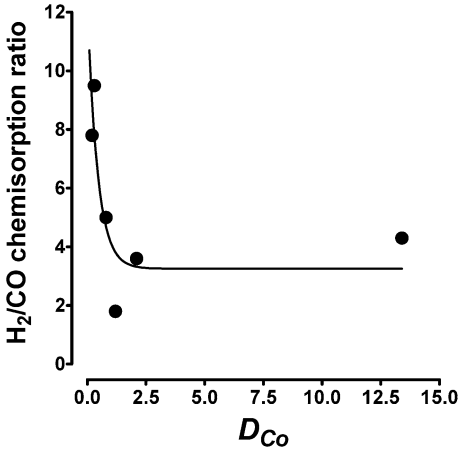

Fig. 9. H_2/CO chemisorption ratio vs Co dispersion.

In the present study, the different catalytic efficiencies of the studied systems cannot be related to either substantial differences in the reduction degree of the active phase (Table 4) or the availability of active metal sites (Table 3), likely due to some synergetic effects of metal dispersion and the ceria carrier. In fact, the plot of site-time-yield against the metal dispersion shown in Fig. 8 exhibits a very sharp decrease in the specific activity of surface Co atoms that cannot be explained in terms of "classical" structure–sensitivity effects [49,52]. In particular, such findings should be related to the different populations of active sites present on the various catalysts, particularly to the prevailing concentration of strong adsorption sites with increasing metal dispersion, implying a marked shift of both CO (Fig. 4A) and H_2 TPD (Fig. 4B) desorption spectra to higher temperatures.

An active role of the ceria carrier on the surface and catalytic properties of the title system is also evident, considering that an increase in metal dispersion actually parallels an increased abundance and availability of surface sites that can adsorb either H_2 or CO molecules (Table 3). Obviously, the effects of the carrier would be enhanced at higher levels of metal dispersion. This is quite evident from data in Fig. 9 showing the relationship between the H_2/CO

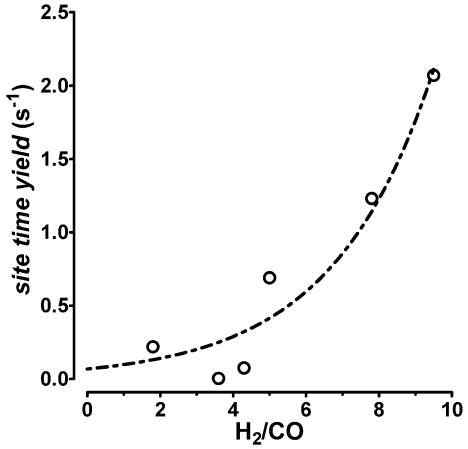

Fig. 10. Site–time–yield vs H_2/CO chemisorption ratio.

chemisorption ratio and Co dispersion, resulting in a similar sharp decrease in the H_2/CO ratio in the 4-*iw* and 4(Urea)-*cb* systems. Therefore, considering the strong surface affinity of the partially reduced ceria for both reactant molecules [23,25,55], the matrix may affect the chemisorption properties of the system, acting as a hydrogen/CO storage system under FTS reaction conditions [25,55]. Therefore, the active role of the matrix in the main reaction pathway would be evident from the increasingly strong relationship between site–time–yield and H_2/CO chemisorption ratio (Fig. 10). This result evidently indicates that changes in metal dispersion affect the chemisorption features of the system in terms of both adsorption strength and relative concentration of sites able to adsorb H_2 and CO molecules. In particular, strong adsorption of the surface intermediates implies lower reactivity, with decreased availability of active H_2 species likely occurring to lower the reactivity of highly dispersed catalysts [55].

5. Conclusions

The physicochemical properties of low-loaded Co/CeO_2 catalysts were investigated and the effects of the preparation method and Co loading on the structure, dispersion and catalytic behavior in the FTS reactions assessed. In particular, the main results of the present study lead to the following conclusions:

- The preparation method markedly affects the structure, reducibility, and dispersion of Co/CeO_2 catalysts.
- The performance of Co/CeO_2 catalysts in the FTS depends on the dispersion of the active phase and Co–CeO_2 metal–support interaction(s).
- A synergetic role of Co and CeO_2 matrix in the chemisorption of reactant molecules controls the reactivity of the title system in the FTS reaction.

References

[1] J. Shen, E. Schmetz, G.J. Kawalkin, J.C. Winslow, R.P. Noceti, M.A. Nowak, D. Krastman, B.J. Tomer, Symposium on Advances in Fischer-Tropsch Chemistry, 219th National Meeting, ACS, San Francisco, 2000.
[2] H. Schulz, Top. Catal. 26 (2003) 1.
[3] H. Fleisch, R.A. Sills, Stud. Surf. Sci. Catal. 147 (2004) 31.
[4] O. Olsvik, R. Ødegård, Stud. Surf. Sci. Catal. 147 (2004) 19.
[5] A. Hoek, L.B.J.M. Kersten, Stud. Surf. Sci. Catal. 147 (2004) 25.
[6] P.J. van Berge, R.C. Everson, Stud. Surf. Sci. Catal. 107 (1997) 207.
[7] G.P. Van der Laan, A.A.C.M. Beenackers, Catal. Rev.-Sci. Eng. 41 (1999) 255.
[8] P. Chaumette, Ph. Coutry, A. Kiennemann, B. Ernst, Top. Catal. 2 (1995) 117.
[9] SASOL International pat., N°PCT/ZA20004/000041.
[10] B. Jager, P. van Berge, A.P. Steynberg, Stud. Surf. Sci. Catal. 136 (2001) 63.
[11] P.K. Bakkerud, J.N. Gol, K. Aasberg-Petersen, I. Dybkjaer, Stud. Surf. Sci. Catal. 147 (2004) 13.
[12] A.P. Steynberg, W.U. Nel, M.A. Desmet, Stud. Surf. Sci. Catal. 147 (2004) 37.
[13] ENI S.p.A. US pat., N°US 20003/0203981 A1.
[14] EU Research project, Contract No. NNE5-2002-00424.
[15] US Research project, Contract No. DE-AC22-94PC94055-13.
[16] R.L. Augustine, Heterogeneous Catalysis for the Synthetic Chemist, Dekker, New York, 1996, p. 153.
[17] E. Iglesia, Appl. Catal. A 161 (1997) 59.
[18] M. Adachi, K. Yoshii, Y.Z. Han, K. Fujimoto, Bull. Chem. Soc. Jpn. 69 (1996) 1509.
[19] A. Kogelbauer, J.G. Goodwin, R. Oukaci, J. Catal. 160 (1996) 125.
[20] R.S. Hurlbut, I. Puskas, D.J. Schumacher, Energy Fuels 10 (1996) 537.
[21] J. van de Loosdrecht, M. van der Haar, A.M. van der Kraan, A.J. van Dillen, J.W. Geus, Appl. Catal. A 150 (1997) 365.
[22] T. Matsuzaki, K. Takeuchi, T. Hanaoka, H. Arakawa, Y. Sugi, K.M. Wei, T.L. Dong, M. Reinikainen, Catal. Today 36 (3) (1997) 311.
[23] A. Trovarelli, Catalysis by Ceria and Related Materials, Imperial College Press, London, 2002, p. 100.
[24] J. Barrault, S. Probst, A. Alouche, A. Percheron-Guegan, V.P. Boncour, M. Primet, Stud. Surf. Sci. Catal. 61 (1991) 357.
[25] B. Ernst, L. Hilaire, A. Kiennemann, Catal. Today 50 (1999) 413.
[26] J.A. Lapszewicz, H.J. Loeh, J.R. Chipperfield, J. Chem. Soc., Chem. Commun. 150 (1993) 913.
[27] E. Iglesia, S.L. Soled, R.A. Fiato, J. Catal. 137 (1992) 212.
[28] E. Iglesia, S.L. Soled, J.E. Baumgartner, S.C. Reyest, J. Catal. 153 (1995) 108.
[29] P. Bera, M.S. Hegde, Catal. Lett. 79 (2002) 75.
[30] P. Bera, A. Gayen, M.S. Hegde, N.P. Lalla, L. Spadaro, F. Frusteri, F. Arena, J. Phys. Chem. B 107 (2003) 6122.
[31] J.F. Moulder, W.F. Stickle, P.E. Sobol, K.D. Bomben, Handbook of X-ray Photoelectron Spectroscopy, Physical Electronics Inc., Eden Prairie, MN, 1995.
[32] F. Arena, G. Gatti, G. Martra, S. Coluccia, L. Stievano, L. Spadaro, P. Famulari, A. Parmaliana, J. Catal. 231 (2) (2005) 365.
[33] F. Arena, F. Frusteri, A. Parmaliana, Appl. Catal. A 187 (1999) 127.
[34] R.C. Reuel, C.H. Bartholomew, J. Catal. 85 (1984) 63.
[35] JCPDS data No. 4-593.
[36] S. Saito, K. Nakahigashi, Y. Shimomura, J. Phys. Soc. Jpn. 21 (1966) 850.
[37] W.L. Roth, J. Phys. Chem. Solids 25 (1964) 1.
[38] F. Giordano, A. Trovarelli, C. de Leitenburg, M. Giona, J. Catal. 193 (2000) 273.
[39] A.M. Hilmen, D. Schanke, A. Holmen, Catal. Lett. 38 (1996) 143.
[40] P. Arnoldy, J.A. Moulijin, J. Catal. 93 (1985) 38.
[41] W.J. Wang, Y.W. Chen, Appl. Catal. 77 (1991) 223.
[42] B.A. Sexton, A.E. Hughes, T.W. Turney, J. Catal. 97 (1986) 390.
[43] R. Brown, M.E. Cooper, D.A. Whan, Appl. Catal. 3 (1982) 177.

[44] A. Boix, E.E. Mirò, E.A. Lombardo, M.A. Bañares, R. Mariscal, J.L.G. Fierro, J. Catal. 217 (2003) 186.
[45] L.A. Bruce, M. Hoang, A.E. Hughes, T.W. Turney, Appl. Catal. A 100 (1993) 51.
[46] P. Bera, S.T. Aruna, K.C. Patil, M.S. Hegde, J. Catal. 186 (1999) 36.
[47] J.T. Richardson, L.W. Wermon, J. Phys. Chem. 62 (1958) 1153.
[48] H. Schulz, Top. Catal. 26 (2003) 73.
[49] S.L. Soled, E. Iglesia, R.A. Fiato, J.E. Baumgartner, H. Vroman, S. Miseo, Top. Catal. 26 (2003) 101.
[50] R.M. de Deugd, F. Kapteijn, J.A. Moulijn, Top. Catal. 26 (2003) 29.
[51] R.C. Reuel, C.H. Bartholomew, J. Catal. 85 (1984) 78.
[52] B.G. Johnson, C.H. Bartholomew, D.W. Goodman, J. Catal. 128 (1991) 231.
[53] K. Sohlberg, S.T. Pantelides, S.J. Pennycook, J. Am. Chem. Soc. 123 (2001) 6609.
[54] H. Pichler, H. Schulz, Chem.-Ing.-Tech. 42 (1970) 1162.
[55] H.B. Shi, Q. Li, X.P. Dai, C.C. Yu, S.K. Shen, Stud. Surf. Sci. Catal. 147 (2004) 313.